Experimental study of the penetrative convection in gases

Valentin Dorel,[*] Patrice Le Gal ⬤, and Michael Le Bars ⬤
CNRS, Aix Marseille Univ, Centrale Marseille, IRPHE, Marseille 13013, France

We present an experimental study of penetrative convection in gases, which allows reaching a lower Prandtl number $Pr = 0.7$ than classical water experiments. A heavy gas (SF_6) fills the bottom of a meter-sized rectangular tank. Diffusion of SF_6 in air establishes a stratified vertical profile in part of the domain. Electric resistors heat the bottom plate of the tank up to a chosen temperature while water circulation fixes the top plate temperature at room temperature. After a short transient, the SF_6-rich lower layer convects and progressively invades the upper stably-stratified layer while exciting propagating internal gravity waves. Density and particle image velocimetry (PIV) measurements are performed, allowing us to follow the growth of the convective region as well as the characteristics of the internal waves and convective fields. While mixing at the interface is often modeled in classical penetrative convection with an eddy diffusivity, we find that the convective layer growths here quadratically in time, which contradicts a stationary and homogeneous turbulent diffusion. The analysis of the wave spectra in the stratified domain reveals a peak frequency at the buoyancy frequency, with a clear cutoff above. Running PIV in both layers simultaneously allows us to compute the kinetic energy transfer from the convective zone into the stratified one, which amounts to about 4%. We also define a scaling law for the erosion rate as a function of the Froude number.

I. INTRODUCTION

Penetrative convection generically stands for the interactions between a turbulent convecting layer of fluid and an adjacent stably-stratified one. It is encountered in many geophysical flows and plays a key role in the deepening of the upper-ocean mixed layer and in the thickening of the layer of suspended sediments in the oceanic benthic boundary layer [1]. It is suspected to occur in the Earth's core and to affect the generation of its magnetic field [2]. Penetrative convection also happens in the atmosphere: its lower part, the troposphere, convects and interacts with the upper part, the stratosphere. This interaction generates waves in the stratosphere, including internal gravity waves (IGWs), whose nonlinear interactions are at the origin of the Quasi-Biennial Oscillation in the equatorial region [3]. In astrophysics, long-time evolution of stars is accessible only through parameterized models that rely on correct physical modeling of small-scale, rapid processes (e.g., [4]). In particular, stars' lifetimes depend on the mixing of their nuclear fuel at the interface between their convective and stratified radiative zones, but stellar convection is strongly turbulent and its interaction with stratified layers through penetrative convection is still difficult to model properly [5]. Also, a full understanding of IGWs excitation and propagation is necessary to take the most of asteroseismology data [6].

In all these examples, full three-dimensional direct numerical simulations are difficult to perform because of the large range of involved temporal and spatial scales. Therefore, submesh

---

[*]dorel@irphe.univ-mrs.fr
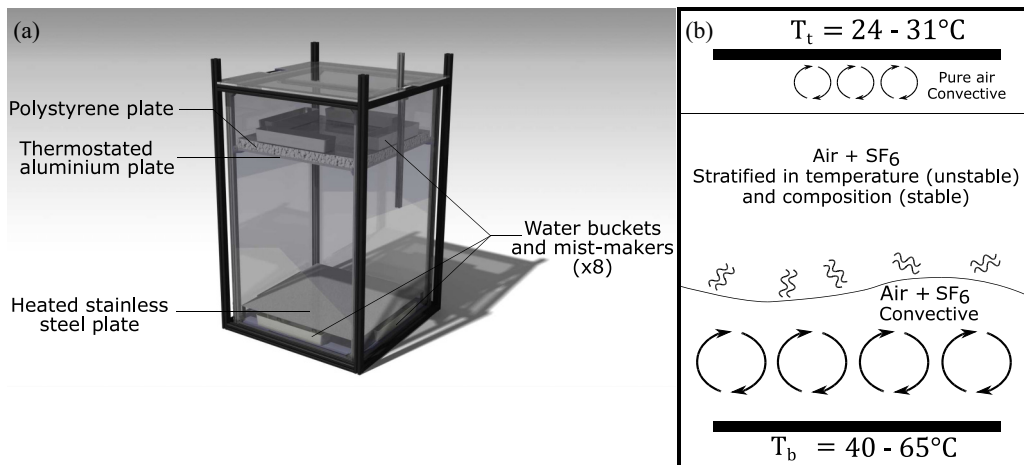
FIG. 1. Sketches of the experimental setup: (a) global rendering (extracted from [14]) and (b) vertical cross section.

parametrization is often used, casting doubts on the relevant quantification of crucial ingredients that determine the long-term behavior of natural systems, such as the amount of energy that transits between the convective and the stratified zones, the amount of mixing at the stratified interface and the invasion speed of the front, etc. The goal of our experimental study is to contribute to the effort of correctly modeling penetrative convection by quantifying the flow motions in the interfacial region. In most experimental studies of penetrative convection to date, water is used as the working fluid, meaning that the Prandtl number $\text{Pr} = \nu/\kappa$, ratio between the fluid viscosity ν and thermal diffusivity κ, is equal to 7 (e.g., [7–9]). Some experiments also use salty water to enhance stratification, then leading to a Schmidt number $\text{Sc} = 700$, equivalent to the Prandtl number but with thermal diffusivity replaced by mass diffusivity (e.g., [10–13]). Those previous experiments are thus fully relevant for oceanic applications, but less relevant for other natural applications where the Prandtl number is smaller than 1, including atmospheres ($\text{Pr} = 0.7$), planetary cores ($\text{Pr} = 0.1$), and stellar interiors ($\text{Pr} = 10^{-8}$). The uniqueness of our experimental setup is that it uses gases and thus reaches $\text{Pr} = 0.7$ and $\text{Sc} = 1.5$. More specifically, we study penetrative convection of a dense gas (sulfur hexafluoride, SF_6) in the overlying air. We stress here that the challenge is to perform quantitative measurements in particular PIV throughout the experiment.

The outline of this article is as follows. We first present in detail the experimental setup and our measurement methods for both velocity and density. In the Results section, we investigate the characteristics of the internal gravity waves produced, the energy transfer from the convective zone into the stratified one, and the growth of the convective layer as well as the entrainment rate at the interface. We finally conclude with the possible outlooks of this experiment.

II. MATERIALS AND METHODS

A. Experimental setup

Our setup is sketched in Fig. 1. The experiment is carried out in a rectangular tank of width $85\,\text{cm} \times 85\,\text{cm}$ and height $150\,\text{cm}$ with $2\,\text{cm}$-thick glass walls. We slowly pour at the bottom a dense gas to produce a stratification with air. We use SF_6, which has a density $\rho_{SF_6} = 6.04\,\text{kg/m}^3 \simeq 5\rho_{\text{air}}$ at ambient temperature $T = 298\,\text{K}$ and pressure $P = 1.013 \times 10^5\,\text{Pa}$, with ρ_{air} the density of pure air. A stainless steel plate is placed at the bottom. It is heated by nine silicone heating pads fixed underneath. The temperature of these pads T_b is maintained constant by a control loop on the pad power supply. The top temperature T_t is fixed at room temperature by an aluminium plate

with internal circulation of a cooling fluid connected to a thermostated bath and isolated from the ambient by a polystyrene plate. The working distance between the two plates is 110 cm. Above the aluminium plate and below the steel one, mist makers are placed in order to produce water droplets which are used as PIV tracers. A fan is placed below the steel plate to homogenize the droplet distribution. The production of water droplets is detailed in Sec. II B 2.

In our setup, as the side walls are not insulated, heat losses through the sides are not negligible. However, we do not expect them to play an important role in the described dynamics. Indeed, the initial room and top aluminium plate temperatures are equal, so the temperature of the gas above the stratified front remains mostly equal to its initial value until the arrival of the penetrative convective bottom layer. Also, all stratified processes are largely dominated by the local SF_6-air composition, with negligible thermal contribution to the buoyancy: so IGWs dynamics do not depend on the details of thermal boundary conditions. Heat losses are important only for the bottom convective layer: in particular, lateral losses may shape a large-scale circulation within the tank, with descending flows near the side boundaries and a rising plume in the vicinity of the tank center. We expect the descending flows and associated temperature fluctuations to remain localized in very thin boundary layers close to the walls, while turbulent fluctuations superimpose to the large-scale circulation and efficiently mix the bulk fluid, in a similar way to classical vertical convection. These points will be further discussed below, where appropriate.

For each of our experiments, the mist makers and the fan are first turned on until the concentration of droplets suitable for PIV is reached. Both the mist makers and the fan are then turned off. Then the bottom of the tank is filled with SF_6. It diffuses upward, creating a vertical stable gradient of density: the longer the diffusion time, the smaller the density gradient but the larger its vertical extension. Once the expected profile is reached, the bottom plate heating is turned on and the gas close to it starts to convect. Figure 1(b) represents the resulting structure. A layer of pure air often remains at the top of the experiment. This layer might also convect, yet less vigorously than the bottom one because both its density and temperature contrast are smaller (i.e., smaller Rayleigh number): we will not further consider it. The bottom convective region mixes with the overlying stratified one and grows with time. We have not observed any signature of double diffusive effects: this makes sense because the Lewis number, the ratio of thermal to mass diffusivities, remains close to 1 (i.e., tabulated value of 2 for a pure SF_6 layer) while the density profile is strongly dominated by the stable, mass contribution vs the unstable thermal one (see details for double diffusive convection threshold in [15]). At the end of the experiment, all the gas in the tank is convecting and fully mixed.

With this setup, we have two main control parameters: the time allowed for mass diffusion before starting the heating, which controls the strength of the stratification, and the amount of heating which controls the strength of the convection. However, it is difficult to precisely explore a wide parameter space. Indeed, the density gradient is only very indirectly controlled, and the accessible temperature difference remains limited to about $30\,°C$, which nevertheless has the advantage of allowing us to neglect compressibility effects and hence to use the Boussinesq approximation in our further modeling.

B. Measurement techniques

1. Density measurements

Density is measured with a densimeter Northdome 2950 from AveniSense. This densimeter slowly moves up and down in the tank, from the bottom steel plate to 71 cm above. The translation speed is 3 mm/s, hence it takes about 4 min to perform a full profile. We record only the downward profiles to minimize possible wake effects. The minimal interval between two profiles is then 8 min. As SF_6 already mixes with air during its initial injection when filling the tank, the density measured at the bottom at the beginning of the experiment is at most $2.51\,kg/m^3$. To validate the density measurements, we performed a purely diffusion experiment: SF_6 is injected at the bottom of the tank and then diffuses upwards with no further perturbation (no convection in this case). Density profiles recorded every 20 min are shown in Fig. 2. Since the molecular agitation energy is large
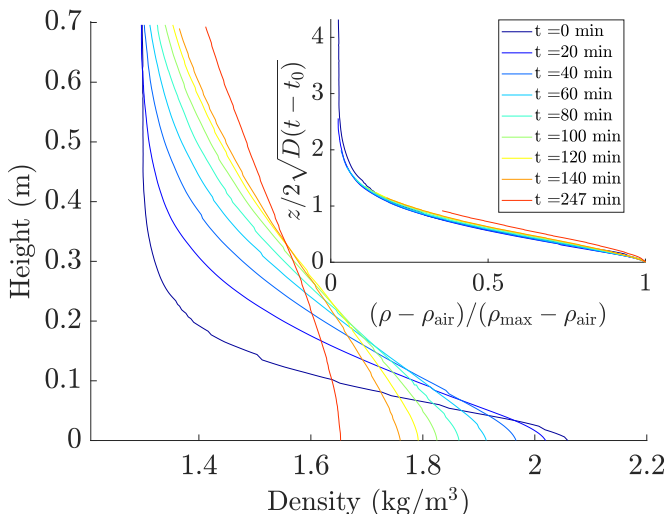
FIG. 2. Density profiles measured with the densimeter Northdome 2950. In the upper right corner the curves are rescaled using the self-similarity of the diffusion process.

enough to oppose the gravity potential energy, we can assume that the density evolution follows the diffusion equation

$$\frac{\partial \rho}{\partial t} = D \frac{\partial^2 \rho}{\partial z^2},\tag{1}$$

where z is the height, t the time, and D the diffusion coefficient of SF_6 in air, whose tabulated value is $D = 1 \times 10^{-5}$ m^2/s. Diffusion is a self-similar process. The corresponding self-similar variable is $z^2/4D(t - t_0)$, t_0 being an adjustable variable to account for the finite duration of the injection process. If we note $\rho_{max}(t)$ the maximum density at time t (i.e., measured at $z = 0$), a self-similar solution to the diffusion equation is

$$\rho(z, t) = \rho_{air} + (\rho_{max}(t) - \rho_{air}) \exp\left(-\frac{z^2}{4D(t - t_0)}\right).\tag{2}$$

Then plotting $z/2\sqrt{D(t - t_0)}$ as a function of $(\rho - \rho_{air})/(\rho_{max} - \rho_{air})$ should gather all the measured profiles as one. All the curves indeed gather using $t_0 = -550$ s. This is shown in Fig. 2, upper right.

The above result is independent of the value of the diffusion coefficient D. To confirm its value, we model each density profile by an high-order polynomial fit, then we calculate the ratio of the left-hand side and the right-hand side of the diffusion equation (1), leading to

$$D = \frac{\partial \rho/\partial t}{\partial^2 \rho/\partial z^2}.\tag{3}$$

As shown in Fig. 3, the histogram of these ratio values resembles a Gaussian centered around $D = (0.9 \pm 0.2) \times 10^{-5}$ m^2/s coherent with the tabulated value, hence validating our density measurements.

2. Water droplets and PIV

Correct seeding to perform PIV in our setup is quite challenging. The idea is to use micrometric water droplets produced by ultrasonic mist makers. Those droplets are small enough to follow the flow without significant sedimentation, and they reflect well the green laser's light. The major problem of this technique is evaporation. Droplets of pure water have a lifetime smaller than 10 min
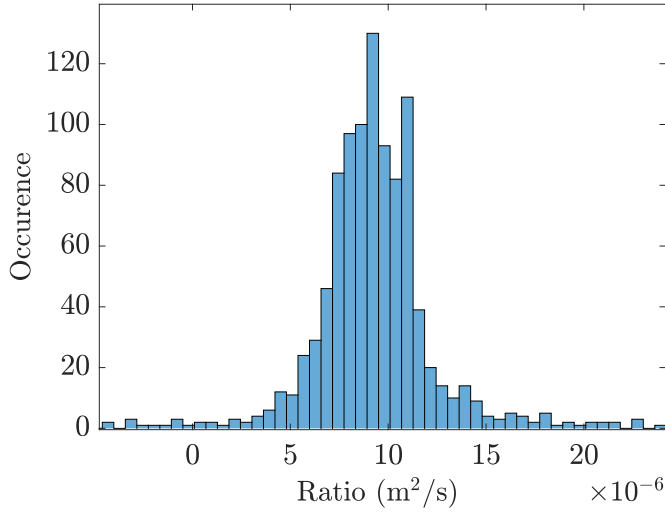
FIG. 3. Histogram of the ratio $(\partial \rho/\partial t)/(\partial^2 \rho/\partial z^2)$ computed from the measured vertical density profiles.

while experiment duration is 1 hour and more. To prevent the droplets from evaporating, we add to the water some UCON oil 75-H-90000, i.e., a miscible glyceryl oil of viscosity $\eta = 44.0\,\text{Pa s}$ at $T = 20\,°\text{C}$. The addition of UCON increases the droplets' lifetime, but also diminishes the quantity of droplets formed by the mist makers; hence there is a good balance to find for optimal PIV measurements. To do so, several water solutions with different proportions of UCON were prepared. A mist maker was immersed in the solution at the bottom of a small $20\,\text{cm} \times 30\,\text{cm} \times 20\,\text{cm}$ tank, illuminated by a vertical laser sheet. For each solution, the mist maker was turned on during 10 s and a camera recorded the formation and evolution of the droplets with time. To analyze the results quantitatively, we made space-time diagrams of a vertical line extracted from the recorded movies, as shown in Fig. 4(a). The intense light at the bottom left corner of the
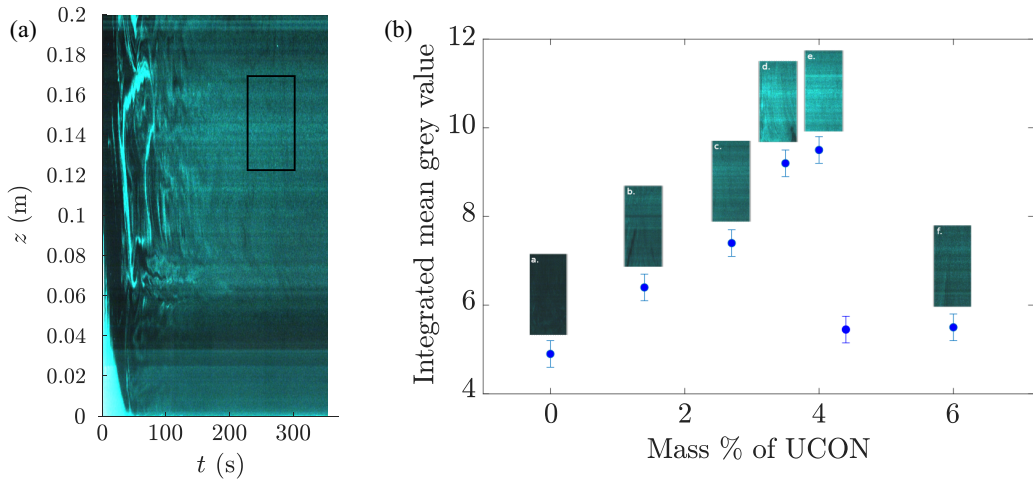
FIG. 4. (a) Typical space-time diagram obtained, with the bottom left corner showing the initial mist creation. The black rectangle shows the zone where the space-time diagrams visible on the systematics in (b) are cropped, and over which the plotted integrated mean gray values of the corresponding grayscale images are computed.
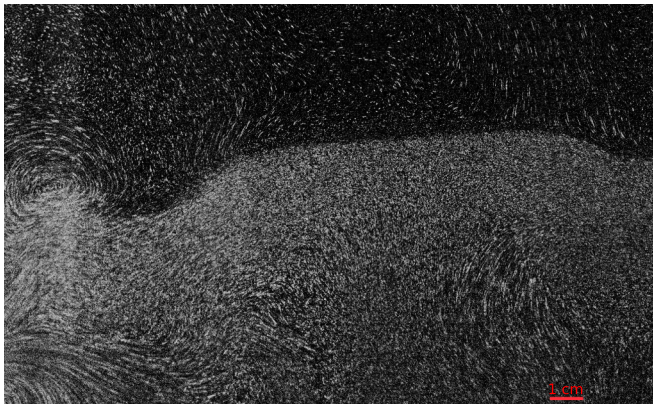
FIG. 5. Average of ten frames acquired during a typical experiment. The convective zone appears with a lighter color hence the interface is clearly visible. The corresponding movie is in the Supplemental Material [17].

picture corresponds to the initial mist creation before the droplets homogenize in the tank. To avoid initial perturbations we crop each space-time diagram in the box shown as a black rectangle, and then calculate the averaged light intensity in the box as a proxy of the drop concentration and persistence. Systematic results are shown in Fig. 4(b). The optimal proportion of UCON oil is between 3.5 % and 4 % in mass. We chose to work with solutions composed of water and 3.5 % of UCON in mass to minimize the quantity of UCON used. With this seeding technique, we managed to perform velocity measurements during more than 3 hours in a row. Note that we do not have direct measurements of our particle sizes, but we can rely on the recent study [16] for an order of magnitude estimate: in the absence of UCON oil, size distribution for their mist maker follows a Gamma distribution with a median droplet size of 5.6 μm. The corresponding typical Stokes falling velocity is about 8.7×10^{-4} m/s, which is negligible compared to typical convective velocities, but not compared to typical velocities recorded in the stratified layer (see below). Actually, as illustrated in Fig. 5, it turns out that there is a strong sedimentation of the particles in the upper layer, where only the smallest ones remain and are passively advected by the IGW field. More and probably larger particles concentrate in the convective region, which allows us to clearly see the interface.

For our PIV measurements, we use a camera of resolution 2048 px × 1536 px, with a 25 mm lens. The chosen frame rate is between 25 and 30 fps and the exposure time is 0.02 s, typical values needed to capture the fast convective motions. The field of view is 15 cm × 20 cm, which is rather small compared to the scale of the experiment; but the droplets are quite small so the camera has to be close to perform PIV. Processing is performed using the open software DPIVSoft 2010 [18]. Careful choice of parameters allows us to compute the PIV simultaneously in the stratified and convective zones. Note that the experiment is transient so the interface crosses the field of view through time.

C. Experiment characteristics

Table I gathers the important characteristics of the experiments presented in this article as well as the figure numbers in which the data are used. The initial bottom density $\rho_{\max}(t = 0)$ and the initial depth of the stratified layer $h_{\text{strat,init}}$ are defined from fitting the first density profile measured at $t = 0$ (see, e.g., the dark blue curve in Fig. 2): $\rho = \rho_{\text{air}} + (\rho_{\max}(t = 0) - \rho_{\text{air}}) \exp(-z^2/h_{\text{strat,init}}^2)$. The associated initial buoyancy (or Brunt-Väisälä) frequency is then computed from the Gaussian

TABLE I. Characteristics of the experiments: top and bottom imposed temperatures, initial bottom density, initial depth of the stratified layer, and associated initial buoyancy frequency.

Experiment	T_t (°C)	T_b (°C)	$\rho_{max}(t=0)$ (kg/m³)	$h_{strat,init}$ (m)	N_{init} (rad/s)	Figure
1	26	45	1.91	0.18	4.1	
2	24	50	2.01	0.14	4.5	8
3	31	40	2.51	0.19	5.0	6, 7, and 9–13

fit at the inflection point of the density profile, using the usual definition

$$N = \sqrt{-\frac{g}{\rho_0}\frac{d\rho}{dz}}, \tag{4}$$

where g is the gravity and ρ_0 a reference density, taken here equal to the air density.

III. RESULTS

A. Internal gravity waves in the stratified region

In this subsection we focus on the stratified zone only. All the presented data come from analyzing images where only the stratified zone is visible.

1. Quantitative validation of the presence of IGWs

The dispersion relation of IGWs is

$$\omega = N\cos\theta, \tag{5}$$

where θ is the angle between the horizontal axis and the wave vector (see, e.g., [19]). This relation gives to IGWs one of their most known unusual behaviours: as $\cos\theta \leqslant 1$, all the energy of the wave field is contained at angular frequencies lower than N. This property can be verified in Fig. 6(a), using data from experiment 3 (see Table I): it shows the periodogram of the vertical velocity v, i.e.,
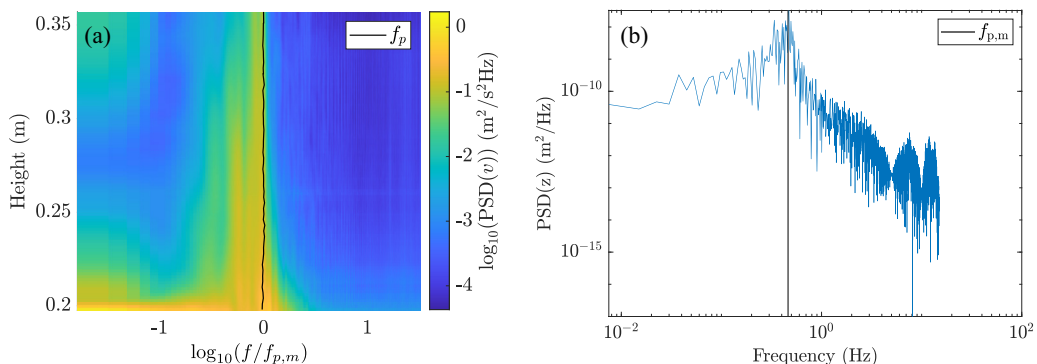
FIG. 6. (a) Periodogram of the vertical velocity v (experiment 3 in Table I). The origin of the height is taken at the bottom steel plate, and the frequency is divided by the depth-averaged Brunt-Väisälä frequency $f_{p,m}$ at the considered time. The black line represents $f_p = N/2\pi$ as a function of height. It appears to be constant in this particular observation. The convective region is just below 0.2 m, and its height does not evolve significantly during the range of times considered. (b) Power spectral density of the vertical displacement z, obtained by integration in the Fourier space of the vertical velocity spectrum.
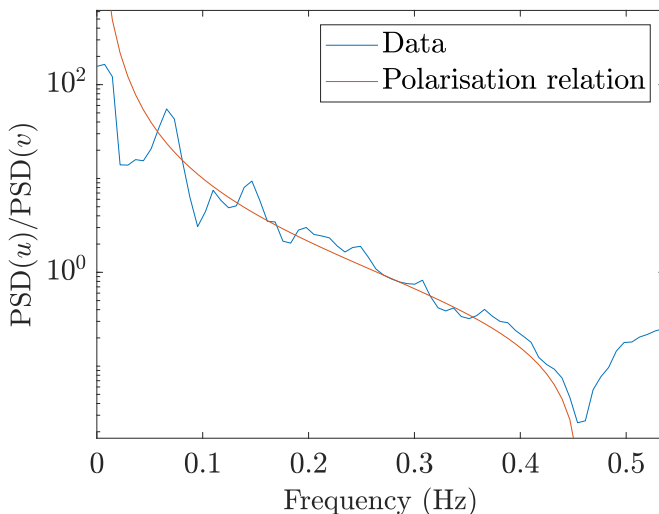
FIG. 7. Theoretical polarization relation (in red) compared with the ratio of the power spectral densities of the horizontal and vertical velocity signals (in blue). The data used here come from the same experiment and same time range as Fig. 6 (experiment 3 in Table I). This comparison has no fitting parameter.

the horizontally averaged spectrum of the vertical velocity signal at each height. It is clear that over the whole studied depth, the energy is contained at angular frequencies lower than N with a clear cutoff, which is coherent with the presence of IGWs.

Ansong and Sutherland [12] studied internal gravity waves generated by a single plume. Using axisymmetric synthetic Schlieren, i.e., a nonperturbative optical technique giving access to the density gradient field, they found that the peak frequency of the vertical displacement spectra lay in a narrow range ($0.45 \leqslant \omega/N \leqslant 0.85$). In order to compare the wave field obtained in our experiment with their results, we integrated the velocity spectrum in Fourier space and produced the power spectral density shown in Fig. 6(b). In our case, the displacement spectrum is peaked around the mean Brunt-Väisälä frequency $f_{p,m}$. Discrepancy in the frequency selection between the two studies probably comes from the difference in the wave excitation mechanism: indeed, wave energy at a given depth is a function of both the energy initially put into that wave during its excitation and of its further damping during its propagation, which depends on its wavelength and frequency.

Another way to confirm the presence of IGWs is the polarization relation, which is straight-forwardly deduced from the dispersion relation coupled to the divergence-free equation for plane waves (see, e.g., [19])

$$\left(\frac{u}{v}\right)^2 = \frac{1}{2}\left[\left(\frac{N}{\omega}\right)^2 - 1\right], \tag{6}$$

where u is the horizontal velocity and the $1/2$ prefactor comes from assuming isotropy in the horizontal plane. This relation holds in Fourier space; then the ratio of the power spectral densities of the horizontal and vertical velocities must follow the same equation. The comparison between our data (averaged in space) and the theoretical polarization relation is presented in Fig. 7: the agreement is striking for a large band of frequencies up to the cutoff buoyancy frequency, with no fitting parameter. This proves that the energy of the flow in the stratified region is carried out almost exclusively by internal gravity waves.
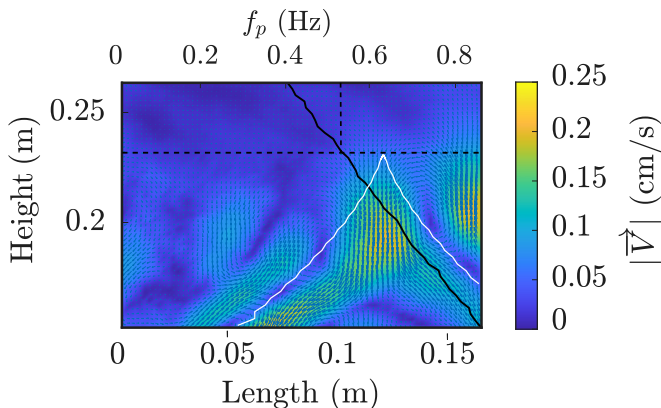
FIG. 8. Snapshot of the filtered velocity signal (experiment 2, Table I). The black curve corresponds to the Brunt-Väisälä frequency $f_p = N/2\pi$ (see the top scale) and is obtained from the vertical density profiles. We consider the mode propagating at a frequency of $f_{filtered} = 0.53$ Hz to the right. The dashed lines point out $f_p = f_{filtered} = 0.53$ Hz and the corresponding height at which IGW reflects. The white line corresponds to an illustrative ray path, computed as a line of constant angular frequency ω in the ambient varying stratification following the dispersion relation (5). The corresponding movie is in the Supplemental Material [17].

2. Mode visualization

To visualize the IGW patterns we can filter the velocity signals. The idea is to filter out the mode propagating at a chosen frequency in a certain direction. The Fourier transform (in both space and time) of the signal is taken. Then we apply a Gaussian filter around the chosen frequency and keep only the signal at $\omega \times k_x > 0$ to select waves propagating with increasing x (see, e.g., [19]). Finally we apply the inverse Fourier transform to the filtered signal.

Data from experiment 2 (Table I) are shown in Fig. 8. The signal is filtered around $f_{filtered} = 0.53$ Hz. This experiment is chosen because N varies greatly with height over the field of view (contrary to experiment 3); hence results illustrate well the properties of internal gravity waves. Figure 8 shows a clear pattern of IGW. As the wave angular frequency ω is constant and N changes with height, the angle θ has to change with height too. The white line shows an example of a ray path, whose normal depth-varying angle θ with the horizontal axis is defined by $\cos\theta = \omega/N$. Isophase lines of the velocity are well fitted by this line, as predicted by the dispersion relation of IGW (5). At height $z = 0.23$ m where $f_p(0.23) = f_{filtered} = 0.53$ Hz, the wave propagates nearly with $\theta = 0$. As the wave cannot propagate in regions where $\omega > N$, it reflects at this height.

3. Energy transfer rate

It is now clear that IGWs propagate in the stratified region. Let us now study how much energy is transferred from the convective zone into the wave field. To compute this quantity, the r.m.s. velocity, computed over the horizontal direction and for 10 seconds, is calculated as a function of height: it exhibits above the interface region a plateau as a function of depth, which we take as the characteristic velocity in the stratified zone $V_{rms,strat}$; it also exhibits just below the interface a maximum, which we take as the characteristic velocity in the convective zone $V_{rms,conv}$. The energy transfer rate τ is then defined as

$$\tau = \frac{\rho_{strat} V_{rms,strat}^2}{\rho_{conv} V_{rms,conv}^2}. \tag{7}$$

Results from experiment 3 (Table I) are shown in Fig. 9. We have positioned the camera in three successive locations, making sure to have a significant part of the convective and stratified
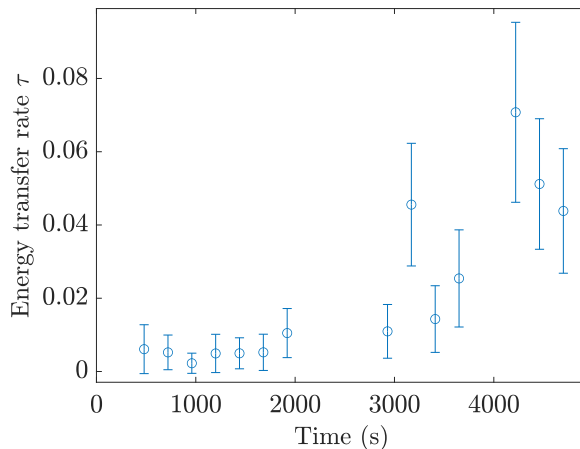
FIG. 9. Energy transfer rate as a function of time for experiment 3 (Table I).

zones in each field of view. The energy transfer rate initially grows with time, while energy accumulates in the stratified region. Rapid changes in the measurements may come from strong fluctuations in the chaotic fluid activity, both in the convective and in the IGW fields. Ansong and Sutherland [12] studied internal gravity waves generated by convective plumes in salted water. Using axisymmetric Schlieren, they studied the energy transferred by the plume into the wave field and found approximately 4 %, which is in the range of observed values at the end of the measurement, when the energy transfer seems to saturate.

B. Growth of the convective region

To quantify the growth of the convective region, the interface height has to be determined at multiple times. The interface can be seen with the camera on the raw images and on the PIV fields, but the field of view of the camera is small ($\sim$20 cm as seen in Fig. 5) . The interface is also visible on the density profiles, which cover a deeper zone ($\sim$70 cm); hence the density profiles are used to determine the interface height. An example is shown in Fig. 10, with results from experiment 3 (Table I). There is a clear mark of the interface on the density profiles, with a constant in depth but time-decreasing density in the turbulent convective zone, and a quasiconstant density gradient ahead. The interface height is defined as the crossing near the point of maximum curvature of the two corresponding tangents. We can see here that diffusion of SF_6 in air is the key to the evolution of the density profile in the stratified region: the density at a given height (0.5 m for example) is changing well before the convection zone reaches this height.

1. Comparison with the classical studies of penetrative convection

The evolution of the interface height with time is shown in Fig. 11. The data are fitted by a power law with initial height, $H = H_0 + a \times t^c$. The fit gives $c = 2.0 \pm 0.1$, corresponding to an interface speed linear in time. The same analysis made in experiment 1 (Table I), with only six density profiles available, gives $c = 1.7 \pm 0.5$, coherent with the first data set. One could worry that the acceleration of the penetration rate with time is related to heat losses from the side; however, two-dimensional numerical simulations in the Boussinesq approximation performed with the same parameters as the experiments, but with no flux lateral boundary conditions, also systematically exhibit a significant acceleration. This behavior is thus generic to our configuration. We focus here on the experiments only, but the systematic numerical study will be the focus of a future work.

Our results do not agree with the historical experiment of Turner [20], who investigated the evolution of a salty layer with linear density profile heated from below with a constant flux. In his
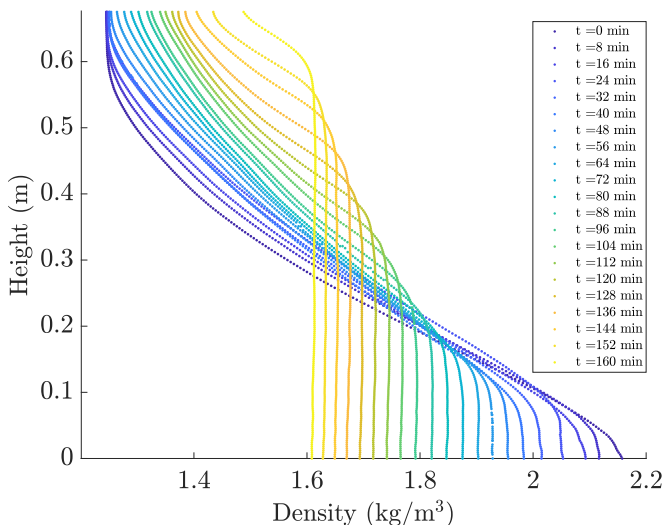
FIG. 10. Vertical density profiles measured every 8 min. The data comes from experiment 3 (Table I). The acquisition rate is 1 Hz, and the densimeter travels downwards at 3 mm/s.

experiment, the interface height grows as $H \propto t^{1/2}$. Fuentes and Cumming [21] did 2D numerical simulations of penetrative convection at low Pr. They impose a constant cooling heat flux F_0 at the top of a domain initially linearly stably stratified, and they also find $H \propto t^{1/2}$. Note that stellar evolution models often use a turbulent diffusivity to model the mixing at the interface, based on the mixing length theory (see, e.g., [4]). The $H \propto t^{1/2}$ growth would correspond to a classical model of eddy diffusivity with a diffusion coefficient constant in space and time.

To understand our specific behavior, we reinvestigate the work of Fernando [22] and Molemaker and Dijkstra [23], who extended the model derived by Turner [20]. We first make the entrainment
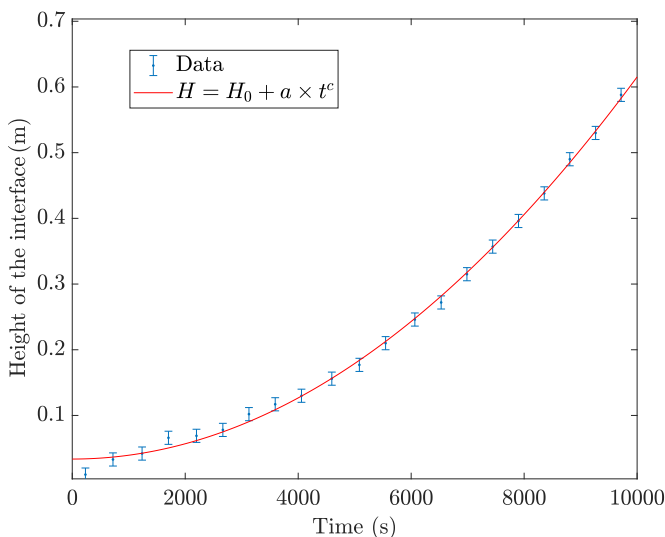
FIG. 11. Growth of the convective zone height for experiment 3 (Table I). The data are fitted with a power law with initial height, $H = H_0 + a \times t^c$, with the best fit giving $c = 2.0 \pm 0.1$.

hypothesis, which supposes that a fraction of the injected thermal energy is converted into kinetic energy, and that part of the kinetic energy of the flow is then transferred into potential energy by mixing the two layers. Noting $E_{\rm p}$ the potential energy, $\mathcal{V}$ the typical convective velocity, $\rho_{\rm c}$ the convective zone density and F_0 the heat flux, we thus have

$$\frac{dE_{\rm p}}{dt} \propto \rho_{\rm c} \mathcal{V}^3 \propto \rho_{\rm c} F_0 H. \tag{8}$$

Where we use the classical scaling for the r.m.s. convective speed $\mathcal{V} \propto (F_0 H)^{1/3}$ [22].

In the classical case [20–23], the density profile in the stratified zone is fixed with a constant buoyancy frequency N in the Boussinesq approximation

$$\rho(z) = \rho_0 - N^2 \frac{\rho_0}{g} z, \tag{9}$$

and by mass conservation the density in the convective zone is

$$\rho_{\rm c} = \rho_0 - N^2 \frac{\rho_0}{g} \frac{H}{2}, \tag{10}$$

which means that a density jump grows at the interface. Straightforward integration up to the maximum height $H_{\rm max}$ gives the potential energy of both the convective and the stratified zones

$$E_{\rm p} = \rho_0 \left(g \frac{H_{\rm max}^2}{2} - N^2 \frac{H_{\rm max}^3}{3} + N^2 \frac{H^3}{12} \right). \tag{11}$$

Then the energy conservation (8) implies

$$\frac{1}{4} \rho_0 N^2 H^2 \frac{dH}{dt} \propto \rho_{\rm c} F_0 H, \tag{12}$$

which with the Boussinesq approximation can be simplified to

$$H \frac{dH}{dt} \propto F_0. \tag{13}$$

A constant flux leads to $H \propto t^{1/2}$ as observed previously [20–23]. In our case however, the initial profile is not maintained, and diffusion plays a key role to rebuild the upfront profile and smooth out any density jump. There we need a different model to understand the time evolution of the density profiles.

2. Model for the density profiles

The hypotheses are the following:

(i) The system is made of two distinct zones: the convective one from $z = 0$ to $z = H(t)$ and the stratified one from $z = H(t)$ to $z = H_{\rm max}$.

(ii) The convective zone has a uniform density $\rho_{\rm c}$.

(iii) The density in the stratified zone is obtained by diffusion from the interface.

Mass conservation in a closed container leads to

$$\int_0^{H_{\rm max}} \rho(z)\, dz = {\rm const} \Rightarrow \frac{d}{dt} \int_0^{H_{\rm max}} \rho(z)\, dz = 0 \Rightarrow \int_0^{H_{\rm max}} \frac{\partial \rho}{\partial t}\, dz = 0. \tag{14}$$

The integral can be split between the two zones

$$\int_0^{H(t)} \frac{d\rho_{\rm c}}{dt}\, dz + \int_{H(t)}^{H_{\rm max}} \frac{\partial \rho}{\partial t}\, dz = 0 \Rightarrow H(t) \frac{d\rho_{\rm c}}{dt} + \int_{H(t)}^{H_{\rm max}} D \frac{\partial^2 \rho}{\partial z^2}\, dz = 0, \tag{15}$$
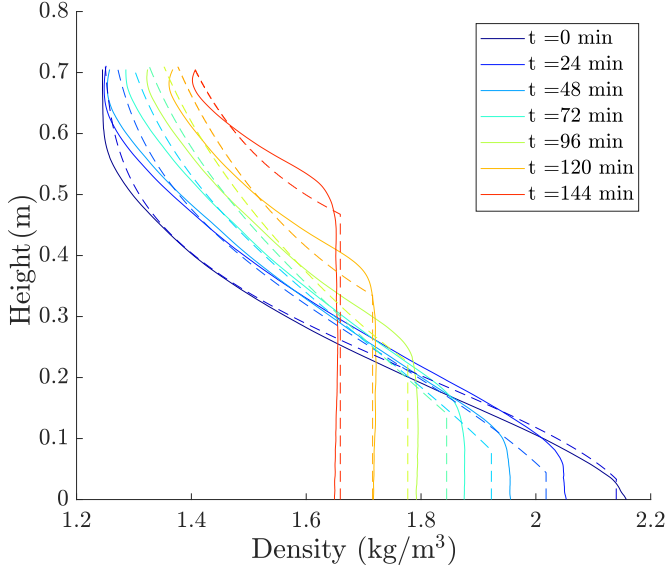
FIG. 12. Comparison between selected experimental density profiles (full line) and the model (dotted line).

so

$$H(t)\frac{d\rho_{\mathrm{c}}}{dt} + D\left(\left.\frac{\partial \rho}{\partial z}\right|_{H_{\max}} - \left.\frac{\partial \rho}{\partial z}\right|_{H(t)}\right) = 0. \tag{16}$$

We suppose there is no mass flux in $z = H_{\max}$ hence $\left.\frac{\partial \rho}{\partial z}\right|_{H_{\max}} = 0$ and

$$\frac{d\rho_{\mathrm{c}}}{dt} = \frac{D}{H(t)}\left.\frac{\partial \rho}{\partial z}\right|_{H(t)}. \tag{17}$$

The system of equations to solve is then

$$\frac{d\rho_{\mathrm{c}}}{dt} = \frac{D}{H(t)}\left.\frac{\partial \rho}{\partial z}\right|_{H(t)} \quad \text{and} \quad \frac{\partial \rho}{\partial t} = D\frac{\partial^2 \rho}{\partial z^2} \quad \text{for} \quad z > H(t). \tag{18}$$

The problem is written out into a matrix formulation. At each time step the diffusion equation is solved with a no-flux condition at the top and continuity of the density at the interface, $H(t)$ being prescribed by experimental measurements. It is integrated in time with the ordinary differential equation solver ode45 in Matlab. The initial condition is the first density profile measured, extrapolated up to the top of the tank by a Gaussian fit.

The model results are compared to the density profiles of experiment 3 (Table I) in Fig. 12, taking the measured value of $H(t)$ and the molecular value of the diffusion coefficient $D = 1 \times 10^{-5}\,\mathrm{m^2/s}$ in the stratified zone. The agreement between the experimental data and the model predictions is overall quite good.

3. Expanded model for the interface growth

The analysis in the previous section shows that the stratification upfront the interface is permanently rebuilt by diffusion. Hence, coming back to the entrainment hypothesis, one can hypothesize that the flux injected in the convective region is used to compensate the increase of potential energy

in the convective region only, equal to

$$\frac{dE_\mathrm{p}}{dt} = \frac{d\rho_\mathrm{c}gH^2/2}{dt} = \rho_\mathrm{c}gH\frac{dH}{dt} + \frac{1}{2}gH^2\frac{d\rho_\mathrm{c}}{dt}. \tag{19}$$

Note again that contrary to the classical model by Fernando [22], we take into account here only the change of potential energy of the convective region. Using (18), the second term can be rewritten

$$\frac{1}{2}gH^2\frac{d\rho_\mathrm{c}}{dt} = \frac{1}{2}gH^2\frac{D}{H}\left.\frac{\partial\rho}{\partial z}\right|_\mathrm{H} \simeq -\frac{\rho_0}{2}DHN^2. \tag{20}$$

We can then compare the order of magnitude of the two terms in the right-hand side of (19) using typical experimental values for dH/dt and N, leading to

$$\frac{\rho_0 DN^2/2}{\rho_\mathrm{c}gdH/dt} \sim 3.5\%. \tag{21}$$

Accordingly neglecting the second term of (19), the conservation equation (8) leads to

$$\rho_\mathrm{c}gH\frac{dH}{dt} \propto \rho_\mathrm{c}F_0H, \tag{22}$$

which implies

$$\frac{dH}{dt} \propto F_0. \tag{23}$$

This is to be compared to the classical scaling (13), the change resulting from the large diffusivity of gas which eradicates any density jump and rebuilds the density profile ahead of the front.

4. Convection scaling laws

Now, we must also consider that in our setup, the bottom temperature—and not the bottom heat flux—is fixed: the next challenge is thus to relate F_0 to H. Many studies have focused on defining scaling laws for the Nusselt number Nu characterizing the heat flux and the Reynolds number Re as a function of the Rayleigh number Ra characterizing the strength of the convection and the Prandtl number Pr (see in particular [24,25]). Classically, those four relevant dimensionless numbers are defined as

$$\mathrm{Nu} = \frac{F_0H}{\lambda\Delta T}, \quad \mathrm{Re} = \frac{\mathcal{V}H}{\nu}, \quad \mathrm{Ra} = \frac{\alpha g\Delta TH^3}{\kappa\nu}, \quad \mathrm{Pr} = \frac{\nu}{\kappa}, \tag{24}$$

where λ is the fluid thermal conductivity, α the thermal expansion coefficient, and ΔT the applied temperature difference. Here we assume that ΔT is constant during the experiment: indeed, the bottom temperature is fixed, and as discussed before, since the initial, ambient, and top temperatures are equal, the upfront temperature remains mostly equal to its initial value until the arrival of the penetrative convective layer. Then a scaling law of the form $\mathrm{Nu} \propto \mathrm{Ra}^\delta$ gives $F_0 \propto H^{3\delta-1}$. With $H \propto t^c$, our relation (23) implies

$$c = \frac{1}{2 - 3\delta}. \tag{25}$$

$1 \leqslant c \leqslant 2$ as measured in our experiment is equivalent to $1/3 \leqslant \delta \leqslant 1/2$, i.e., to a Nusselt scaling between the regimes IV_u and IV_l defined by Grossmann and Lohse [24]. Note that we interpret here the dynamics of our penetrative convective layer with results coming from the classical Rayleigh-Bénard configuration. We thus somehow assume that heat losses in our setup shape a large-scale circulation on which turbulent fluctuations superimpose. These turbulent fluctuations are assumed to be similar to the classical case and to be responsible for the vertical heat and momentum transfers.

Actually, Grossmann and Lohse [24] predict analytically all regimes of the Nu-Ra relation depending on the values of Ra and Pr in the classical Rayleigh-Bénard setting. An estimation of

the Rayleigh number in our setup gives $10^7 < \text{Ra} < 10^9$ at intermediate times, with $\text{Pr} = 0.7$. For these values, the relevant scaling in the classical Rayleigh-Bénard setting would be $\text{Nu} \propto \text{Ra}^{1/4}$ corresponding to regime I_l. However, our setup differs significantly from the Rayleigh-Bénard convection: in particular, the boundary close to the stratified interface is not rigid, nor even free-slip, since it can freely move. Therefore, we might speculate that the flux through this free-moving boundary is not controlled by the bottom diffusive boundary layer. We argue that dissipation there might be dominated by bulk dissipation for both momentum and heat, as in regime IV of Grossmann and Lohse. Furthermore, since in our case $\text{Pr} < 1$, the thermal boundary layer is thicker than the viscous one. This would correspond to the regime IV_l for which $\text{Nu} \propto \text{Ra}^{1/2}$.

It might seem surprising to observe this regime at not so high Rayleigh numbers reached in our setup. Indeed, the $1/2$ scaling between Nu and Ra corresponds to the so-called ultimate regime, where the heat flux is independent of the diffusive processes (viscosity and thermal diffusivity). The existence of the ultimate regime in Rayleigh-Bénard convection is still debated, even at much larger Ra. Funfschilling *et al.* [26] searched this ultimate regime in a meter-sized tank filled with gas. Their data are coherent with the work of Niemala *et al.* [27], and neither observed the transition to the ultimate regime described by Chavanne *et al.* [28] close to $\text{Ra} \sim 10^{11}$. Yet this ultimate regime was observed by Lohse and Toschi [29] in a numerical simulation of bulk turbulent convection, with no boundaries. Then, the $1/2$ scaling law between Nu and Ra is observed at Rayleigh numbers as low as $\text{Ra} \sim 1 \times 10^6$. The $1/2$ scaling law has also been experimentally observed by Lepot *et al.* [30] at Rayleigh numbers comparable to ours, using an original setup where convection is driven by radiative heating, so that the fluid is heated internally and boundary layers are bypassed. This might also be the case in our setup. Additional data are necessary to definitely confirm our conclusion. But considering the regime IV_l scaling with $\delta = 1/2$ leads to $c = 2$, i.e., an interface growing quadratically in time, as observed in our best-quality measurements (see Fig. 11). Note, however, that this best-quality measurements experiment is also our most extreme case, and that our second, less precise determination from experiment 1 (see Table I) gives $c = 1.7$ corresponding to $\delta = 0.47$. Our main point here is that in all cases, the penetration rate in our setup increases with time, which is well interpreted by any Nu-Ra scaling exponent between the classical $1/3$ and the limit $1/2$. We do not claim here that we have proven that our flow satisfies the ultimate regime of convection. Yet, a nonclassical exponent for the scaling law Nu(Ra) is indeed needed to explain the convective front acceleration, a fact that we relate to the absence of a classical boundary layer at the convective-stratified interface.

C. Entrainment rate and Froude number

Another way to evaluate the efficiency of penetrative convection is to quantify its entrainment rate

$$E = \frac{dH/dt}{\mathcal{V}} \tag{26}$$

and relate it to the Froude number

$$\text{Fr} = \frac{\mathcal{V}}{Nl}. \tag{27}$$

Here $\mathcal{V}$ is a typical convective velocity at a corresponding scale l. The variation of E with Fr has been investigated in various situations with different momentum sources in two-layer, turbulent/stably stratified systems: oscillating grids, jets, plumes, etc. The initial hope was to define a universal scaling law relating E and Fr, independent of the source of turbulence. Fernando [1] in his review in 1991 concluded that after 50 years of research, there was no consensus on any scaling law. Shrinivas and Hunt in 2014 [31] confirmed that this was still the case, as illustrated in Fig. 13 reproduced from their work, where for the same Fr, measured entrainment rates from different groups and setups differ by more than one order of magnitude.
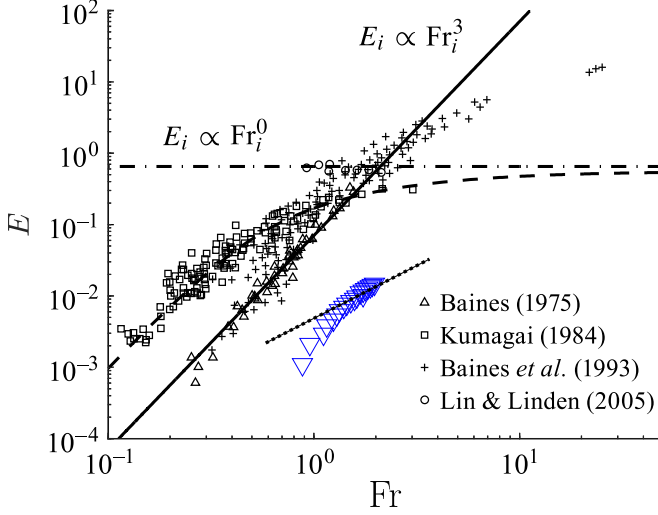
FIG. 13. Entrainment rate E as a function of the Froude number. This figure is reproduced from Fig. 1 of [31] and collects data from [10,33] using an axisymmetric turbulent plume impinging a density jump, and from [11,34] using a turbulent fountain impinging a density jump. Blue triangles correspond to our data from experiment 3 (Table I). The dotted line shows the 3/2 power law towards which our data converge, a trend also visible on the data of [34] (plus symbols).

We assume first that the buoyancy flux in the convective region $q_0 = F_0 \alpha g / \rho_c C_p$ is actually equal to the dissipation rate ϵ of the Kolomogorov turbulence, with C_p the gas heat capacity. Then $q_0 = \mathcal{V}^3 / l$ is a constant at each scale down to the mixing scale. Following the Kolmogorov-type approach described in [32], mixing occurs when the local Péclet number is of order one. Noting V_m and l_m the typical speed and length at mixing scale,

$$\mathrm{Pe}_l = \frac{V_m l_m}{D} = 1, \quad \text{with} \quad V_m = (q_0 l_m)^{1/3}. \tag{28}$$

l_m is referred to as the Obukhov-Corrsin scale in the literature. Then

$$l_m = D^{3/4} q_0^{-1/4} \quad \text{and} \quad V_m = D^{1/4} q_0^{1/4}, \tag{29}$$

and the Froude number at the mixing scale Fr_m is

$$\mathrm{Fr}_m = \frac{V_m}{N l_m} = \frac{q_0^{1/2}}{N D^{1/2}}. \tag{30}$$

Let us now suppose a mixing law of the form

$$E = \mathrm{Fr}_m^\beta, \tag{31}$$

which corresponds to

$$\frac{dH}{dt} = V_m \mathrm{Fr}_m^\beta = N^{-\beta} D^{1/4 - \beta/2} q_0^{1/4 + \beta/2}. \tag{32}$$

The model of interface growth from the previous section gives

$$H = a \times t^2 \quad \text{and} \quad q_0 = \frac{\alpha g}{\rho c_p} F_0 = \frac{\alpha g}{\rho c_p} 3.4 \times 10^{-3} \frac{\lambda \Delta T}{H} \mathrm{Ra}^{1/2} \mathrm{Pr}^{1/2}, \tag{33}$$

where the numerical constant in the flux equation comes from the updated prefactors in [25] for the ultimate regime IV_l. Replacing in (32) gives $\beta = 3/2$, which is in the range of previously observed

scaling exponents for the entrainment rate, typically $0 \leqslant \beta \leqslant 3$ as shown in Fig. 13. We also show our measurements taking the calculated V_m and l_m at each time, which are respectively in the range [5.1–7.7] mm/s and [1.9–1.3] mm. Dispersion in the results compiled in Fig. 13 comes from the very different setups encompassing, e.g., various extensions of the turbulent source (local for jets and plumes vs over the whole width for us) and various types of stratification (density jump vs linear stratification). The search for a universal E-Fr scaling would require a uniform definition of the relevant velocity and length scales for the mixing.

IV. CONCLUSION

In conclusion, we have studied experimentally the penetrative convection in gases, reaching a Pr < 1 more relevant to atmospheric, planetary, and astrophysical flows. Flows in the stratified region have been studied: the results found are coherent with the properties of internal gravity waves. Their energy lies at frequencies $\omega < N$ only, the polarization relation is verified on a large band of frequencies, and by filtering PIV signals we recover the geometric properties of IGW. The convective zone transfers energy to the stratified one, which accumulated up to 4 % in proportion. The height of the convective zone grows parabolically with time, in contradiction with the classically observed evolution as a square root of time, which echoes a parametrization of mixing by some turbulent diffusion. Different models are to be expected depending on the Prandtl number and boundary conditions. Here an explanation of the measured squared-time evolution is proposed, relying on an adapted version of the analytical model of Fernando [22] and on the convection scaling laws of Grossmann and Lohse [24]. This model translates into a different scaling law for the mixing efficiency, with a $Fr^{3/2}$ dependency. All the results presented here rely on a limited set of experimental data, because performing measurements in our unstationary setup in gas remains very challenging, and because our configuration does not allow an easy and systematic exploration of the parameter space. All experiments were also performed with non-negligible side heat losses. Additional studies are thus necessary to confirm the trends proposed here, including improved experiments and complementary numerical simulations, following, for instance, the recent work by [21].

ACKNOWLEDGMENTS

---

[1] H. J. S. Fernando, Turbulent mixing in stratified fluids, Annu. Rev. Fluid Mech. **23**, 455 (1991).

[2] M. Bouffard, B. Favier, D. Lecoanet, and M. Le Bars, Internal gravity waves in a stratified layer atop a convecting liquid core in a non-rotating spherical shell, Geophys. J. Int. **228**, 337 (2022).

[3] R. A. Plumb, The interaction of two internal waves with the mean flow: Implications for the theory of the quasi-biennial oscillation, J. Atmos. Sci. **34**, 1847 (1977).

[4] B. Paxton, L. Bildsten, A. Dotter, F. Herwig, P. Lesaffre, and F. Timmes, Modules for experiments in stellar astrophysics (MESA), Astrophys. J. Suppl. Ser. **192**, 3 (2011).

[5] E. H. Anders, A. S. Jermyn, D. Lecoanet, and B. P. Brown, Stellar convective penetration: Parameterized theory and dynamical simulations, Astrophys. J. **926**, 169 (2022).

[6] P. Edelmann, R. Ratnasingam, M. Pedersen, D. Bowman, V. Prat, and T. Rogers, Three-dimensional simulations of massive stars. I. Wave generation and propagation, Astrophys. J. **876**, 4 (2019).

[7] J. W. Deardorff, G. E. Willis, and D. K. Lilly, Laboratory investigation of non-steady penetrative convection, J. Fluid Mech. **35**, 7 (1969).

[8] A. A. Townsend, Natural convection in water over an ice surface, Q. J. R. Meteorolog. Soc. **90**, 248 (1964).

[9] P. Léard, B. Favier, P. Le Gal, and M. Le Bars, Coupled convection and internal gravity waves excited in water around its density maximum at 4 °C, Phys. Rev. Fluids **5**, 024801 (2020).

[10] W. D. Baines, Entrainment by a plume or jet at a density interface, J. Fluid Mech. **68**, 309 (1975).

[11] Y. J. P. Lin and P. F. Linden, The entrainment due to a turbulent fountain at a density interface, J. Fluid Mech. **542**, 25 (2005).

[12] J. K. Ansong and B. R. Sutherland, Internal gravity waves generated by convective plumes, J. Fluid Mech. **648**, 405 (2010).

[13] J. Herault, G. Facchini, and M. Le Bars, Erosion of a sharp density interface by a turbulent jet at moderate Froude and Reynolds numbers, J. Fluid Mech. **838**, 631 (2018).

[14] P. Léard, On the interaction between turbulence and stratification: Penetrative convection, internal gravity waves and large-scale flow generation: Geophysical and astrophysical applications, Ph.D. thesis, Aix-Marseille (2020).

[15] P. Garaud, Double-diffusive convection at low Prandtl number, Annu. Rev. Fluid Mech. **50**, 275 (2018).

[16] S. Kooij, A. Astefanei, G. L. Corthals, and D. Bonn, Size distributions of droplets produced by ultrasonic nebulizers, Sci. Rep. **9**, 6128 (2019).

[17] See Supplemental Material at http://link.aps.org/supplemental/10.1103/PhysRevFluids.8.103501 for the movie of an experiment and a movie of internal gravity wave propagation.

[18] P. Meunier and T. Leweke, Analysis and treatment of errors due to high velocity gradients in particle image velocimetry, Exp. Fluids **35**, 408 (2003).

[19] B. R. Sutherland, *Internal Gravity Waves* (Cambridge University Press, Cambridge, 2010).

[20] J. S. Turner, The behaviour of a stable salinity gradient heated from below, J. Fluid Mech. **33**, 183 (1968).

[21] J. R. Fuentes and A. Cumming, Penetration of a cooling convective layer into a stably-stratified composition gradient: Entrainment at low Prandtl number, Phys. Rev. Fluids **5**, 124501 (2020).

[22] H. J. S. Fernando, The formation of a layered structure when a stable salinity gradient is heated from below, J. Fluid Mech. **182**, 525 (1987).

[23] M. J. Molemaker and H. A. Dijkstra, The formation and evolution of a diffusive interface, J. Fluid Mech. **331**, 199 (1997).

[24] S. Grossmann and D. Lohse, Scaling in thermal convection: A unifying theory, J. Fluid Mech. **407**, 27 (2000).

[25] R. J. A. M. Stevens, E. P. van der Poel, S. Grossmann, and D. Lohse, The unifying theory of scaling in thermal convection: The updated prefactors, J. Fluid Mech. **730**, 295 (2013).

[26] D. Funfschilling, E. Bodenschatz, and G. Ahlers, Search for the "ultimate state" in turbulent Rayleigh-Bénard convection, Phys. Rev. Lett. **103**, 014503 (2009).

[27] J. J. Niemela, L. Skrbek, K. R. Sreenivasan, and R. J. Donnelly, Turbulent convection at very high Rayleigh numbers, Nature (London) **404**, 837 (2000).

[28] X. Chavanne, F. Chillà, B. Castaing, B. Hébral, B. Chabaud, and J. Chaussy, Observation of the ultimate regime in Rayleigh-Bénard convection, Phys. Rev. Lett. **79**, 3648 (1997).

[29] D. Lohse and F. Toschi, Ultimate state of thermal convection, Phys. Rev. Lett. **90**, 034502 (2003).

[30] S. Lepot, S. Aumaître, and B. Gallet, Radiative heating achieves the ultimate regime of thermal convection, Proc. Natl. Acad. Sci. USA **115**, 8937 (2018).

[31] A. B. Shrinivas and G. R. Hunt, Unconfined turbulent entrainment across density interfaces, J. Fluid Mech. **757**, 573 (2014).

[32] H. Tennekes, *A First Course in Turbulence* (MIT Press, Cambridge, MA, 1972).

[33] M. Kumagai, Turbulent buoyant convection from a source in a confined two-layered region, J. Fluid Mech. **147**, 105 (1984).

[34] W. D. Baines, A. F. Corriveau, and T. J. Reedman, Turbulent fountains in a closed chamber, J. Fluid Mech. **255**, 621 (1993).